Atmos. Meas. Tech. Discuss., 7, 769–817, 2014
www.atmos-meas-tech-discuss.net/7/769/2014/
doi:10.5194/amtd-7-769-2014

Atmospheric Measurement Techniques
Discussions
Open Access

A permanent raman lidar station in the Amazon: description, characterization and first results

H. M. J. Barbosa[1], B. Barja[2], T. Pauliquevis[3], D. A. Gouveia[1], P. Artaxo[1], G. G. Cirino[4], R. M. N. Santos[5], and A. B. Oliveira[6]

[1]Instituto de Física, Universidade de São Paulo, Rua do Matão, Travessa R, 187. 05508-090, São Paulo, S.P., Brazil
[2]Centro Meteorológico de Camagüey, Instituto de Meteorología de Cuba, Cuba
[3]Depto. de Ciências Exatas e da Terra, UNIFESP, Diadema, S.P., Brazil
[4]Instituto Nacional de Pesquisas da Amazônia, Manaus, A.M., Brazil
[5]Universidade do Estado do Amazonas, Manaus, A.M., Brazil
[6]Instituto Federal de Educação, Ciência e Tecnologia de São Paulo, São Paulo, S.P., Brazil

Received: 31 December 2013 – Accepted: 16 January 2014 – Published: 28 January 2014

Correspondence to: H. M. J. Barbosa (hbarbosa@if.usp.br)

Published by Copernicus Publications on behalf of the European Geosciences Union.

Abstract

A permanent UV Raman Lidar station, designed to perform continuous measurements of aerosols and water vapor and aiming to study and monitor the atmosphere on the weather to climatic time scales, became operational in central Amazon in July 2011. The automated data acquisition and internet monitoring enabled extended hours of daily measurements when compared to a manually operated instrument. This paper gives a technical description of the system, presents its experimental characterization and the algorithms used for obtaining the aerosol optical properties and identifying the cloud layers. Data from one week of measurements during the dry season of 2011 were analyzed as a mean to assess the overall system capability and performance. A comparison of the aerosol optical depth from the Lidar and a co-located AERONET sun photometer showed a root mean square error of about 0.06, small compared to the range of observed AOD values (0.1 to 0.75) and to the typical AERONET AOD uncertainty (0.02). By combining nighttime measurements of the aerosol lidar ratio (50–65 sr), backtrajectories calculations and fire spots observed from satellites we showed that observed particles originated from biomass burning. Cirrus clouds were observed in 60 % of our measurements. Most of the time they were distributed into three layers between 11.5 and 13.4 km a.g.l. The systematic and long-term measurements being made by this new scientific facility have the potential to significantly improve our understanding of the climatic implications of the anthropogenic changes in aerosol concentrations over the pristine Amazônia.

1 Introduction

Amazonia is under continuous and constant changes in land use, with important climatic implications (Davidson and Artaxo, 2004). Aerosol concentrations vary from pristine conditions at very low concentrations to heavy loaded conditions, similar to polluted urban areas, following the seasonal cycle of deforestation and biomass burning

(Artaxo et al., 2013). These large biomass burning emissions overlap with continuous urban emissions in regions near large metropolitan areas, such as downwind from Manaus (Kuhn et al., 2010). These high concentrations of aerosols and trace gases play an important role in the atmospheric composition, convection, cloud formation and the precipitation regimes (Andreae et al., 2004; Koren et al., 2012), having been even linked to a delay on the wet season onset (Bevan et al., 2009; Butt et al., 2011). To fully understand the climatic implications of the anthropogenic changes in aerosol concentrations over the pristine Amazonia, the vertical distribution of the aerosol optical properties need to be known, with long term measurements coupled with ground based and satellite remote sensing. This is critically important to help understanding the interaction of aerosol particles with clouds in tropical regions (Freud et al., 2008; Feingold, 2003). Clouds and aerosols affects strongly the radiation balance (Forster et al., 2007) and it was shown that in Amazonia the cloud cover and aerosol loading has important impacts in the radiation balance as well as in carbon uptake by the vegetation (Oliveira et al., 2007; Cirino et al., 2013).

Measurements of the vertical profile of aerosols in the Amazon region started in the dry season of 1985 during the Amazon Boundary Layer Experiment (ABLE2) campaign (Harriss et al., 1988) when an airborne DIfferential Absorption Lidar (DIAL) was used. Andreae et al. (1988) found smoke and haze layers up to 5 km, frequently distributed in multiple layers. The first campaign to use a standard aerosol Lidar was the Smoke, Clouds and Radiation – Brazil (SCAR-B) (Kaufman et al., 1998). The downward looking Lidar onboard the aircraft revealed the spatial structure of plumes with and without cloud activity. Using airborne measurements during the same campaign, Reid et al. (1998) reported a second temperature inversion between 2 and 4 km, corresponding to the top of the convective layer, trapping the aerosol layer below it. These results revealed a very complex aerosol vertical structure, with implications in the vertical temperature profile.

Some intensive campaigns relied only on airborne in situ instrumentation for assessing the vertical distribution. For instance, during the dry season of 1992, the

Transport and Atmospheric Chemistry Experiment-A (Pereira et al., 1996, TRACE-A) campaign performed six flights for measuring the vertical distribution of biomass burning aerosol. The maximum particle mass concentration of about 15 000 cm^{-3} was found near the temperature inversions around 2.5 km. The Cooperative Large Scale Biosphere–Atmosphere (LBA) Regional Experiment (CLAIRE-98) was the first large campaign during the wet season and measurements were taken with a Brazilian Bandeirante plane over northern Amazon (Formenti et al., 2001). Two days with strong impact of Saharan dust aerosols were identified in a layer extending from the ground to 3.5 km. Some measurements showed an unexpected increase of trace gases concentrations above 10 km. Employing back trajectories calculations, Andreae et al. (2001) concluded that it originated from savanna fires further downwind that were vertically transported by deep convection and brought equatorward by the upper level circulation. Analysis of aerosol size distributions indicated a possible formation of new particles near the detrainment zone of deep convection (Krejci et al., 2003). Latter, the LBA – Smoke, Aerosols, Clouds, Rainfall and Climate (LBA-SMOCC) campaign found aerosol scattering increasing with altitude by a factor of 2 to 10, which Chand et al. (2006) attributed to the aging of biomass burning particles. From the same experiment, Guyon et al. (2005) showed that as aerosols are transported above the mixing layer the particle number concentration was reduced by only 20 % while the particle size increased. The authors concluded that the transport by non-precipitating shallow clouds were the most important.

The first relatively long term ground based Lidar observations in central Amazon took place during the European Integrated Project on Aerosol, Cloud, Climate, Air Quality Interactions, (EUCAARI, Kulmala et al., 2011) and the Amazonian Aerosol Characterization Experiment (AMAZE-08, Martin et al., 2010). From 10 months of observations in 2008, Baars (2011) analyzed 60 wet and 55 dry season days where meteorological and instrumental conditions were optimal. In a more detailed study, Baars et al. (2011) identified both the transport of Saharan dust and/or biomass burning from Africa in 32 % of their wet season observations, thus confirming previous findings of sporadic intrusions of Saharan dust (Talbot et al., 1990; Formenti et al., 2001) and African fires (Kaufman et al., 2005). The authors were able to quantify the contribution and compute the aerosol optical depth (AOD) for smoke and biomass burning aerosols separately, showing that at least for half of these cases African biomass burning dominated the total AOD. The long-range transport occurred below 3.5 km, while in clean conditions the biogenic aerosols were found to be trapped below 2 km. Baars et al. (2012) showed that column AOD, the maximum extinction and backscatter coefficients during the dry season were about three times higher than during the wet season of 2008. Moreover, an analysis of biomass burning plumes heights indicated that the convective mixing by pyro or deep cumulus was determinant for the vertical distribution of aerosols, indicating the important role of aerosol-cloud interactions in tropical regions (Boucher et al., 2013).

As can be noted from the previous discussion, the vertical distribution of the aerosol optical properties in the Amazon is known only during limited time periods, therefore not allowing for a climatological perspective as well as a clear picture of the strong seasonality characteristic of tropical regions. To overcome this lack of knowledge, a permanent UV Raman Lidar station was implemented in central Amazon in mid-2011 aiming to study and monitor the vertical distribution of aerosols, water vapor and also study the aerosol-clouds interactions. This paper reports on this new instrument, its first measurements and results. Section 2 gives the system description and discusses its characterization and analysis algorithm is presented in Sect. 3. Section 4 presents the first results from one week of intensive measurements in September 2011. Finally, in Sect. 5 conclusions and future work are discussed.

2 Instrument description and performance

The site is located up-wind from the city of Manaus-AM, Brazil, inside the campus of Embrapa Amazônia Ocidental at 2.89° S 59.97° W and 100 m altitude. This new experimental site was implemented in 2011 and planned to run continuously during the

next years applying a synergy of different instruments to help understanding the interactions and feedback mechanisms between humidity, convection, clouds and aerosols (Pauliquevis et al., 2014). It was initially implemented by the FAPESP (Fundação de Amparo a Pesquisa do Estado de São Paulo) project – Direct and indirect effects of aerosols on climate in Amazonia and Pantanal (Artaxo et al., 2013), but also received contribution from FAPESP project – Cloud processes of the main precipitation systems in Brazil: a contribution to cloud resolving modeling and to the GPM (Machado et al., 2014), the project Amazonian Dense GNSS Meteorological Network (Adams et al., 2011). More recently, a contribution from the Max Planck Institute in Hamburg added critical instrumentation. Among the instruments included are Lidar, ceilometer, sunphotometer, multi-filter radiometer, nephelometer, aethalometer, weather station, disdrometer, vertical pointing rain radar and water vapor column using GNSS. This paper focus mostly on the characterization and first results obtained with the Raman Lidar, further described below. Data from collocated and nearby operational soundings are also used. For the validation of the optical properties derived from the Lidar measurements, aerosol optical depth from the collocated Aerosol Robotic Network (AERONET) station (Holben et al., 1998) is used.

The Lidar system LR-102-U-400/HP was manufactured by Raymetrics Advanced Lidar Systems, in Greece. It uses a Quantel CFR-400 Nd-YAG laser at 355 nm with 95 mJ per pulse and 10 Hz repetition rate. The beam is expanded by a factor of 4 and final laser divergence is 0.36 mrad. The optical system is bi-axial with a 300 mm separation between the Cassegrain telescope and the laser axis, which is tilted by 0.28 mrad towards the first. The primary mirror of the telescope has 400 mm diameter, while the secondary has 90 mm. Focal length is 4000 mm resulting in a f/10 system. The diameter of the iris used at the focal plane can be changed, allowing the telescope field of view to be adjusted between 0.25 and 3 mrad. No optical fibers are used and light passing through the iris goes directly to the optical elements in the detection box. A pair of convergent lens produces a parallel beam with 8 mm diameter. Three partial reflecting mirrors separate the elastic back scattered signal and the inelastic signals due to the Raman cross-section of N_2 (387 nm) and H_2O (408 nm). Interferometric filters with 1 nm FWHM before each photomultiplier tube reduce the background noise. For the elastic channel, a neutral density filter is used to attenuate the signal and avoid saturation. Light signals are measured with Hamamatsu R9880U-210 photomultiplier tubes (PMT).

Data acquisition is based on the Licel Transient Recorder model TR-20-160 manufactured by Lidar Computing and Electronics (Licel) GmbH. This integrated optical detection system combines analog (AN) and single photon counting (PC) measurements. The 12-bit analog to digital converter (ADC) process data from the 355 and 387 nm signals at 20 MHz, yielding a raw resolution of 7.5 m. The ADC scale can be set to 20, 100 or 500 mV, corresponding to a resolution of 0.005, 0.024 and 0.122 mV. Photon counting is performed at 250 MHz for the 355, 387 and 408 nm signals. The simultaneous measurement in analog and photon count modes allows extending the dynamical range of the instrument, making it possible to measure from ~ 500 m to above 15 km with a single telescope.

Due to the analog to digital converter bandwidth and pipelining, a time delay between the AN and PC is expected. For measuring this delay, 60 profiles with 600 shoots each were used. A linear regression between AN and PC data were performed using only the region were both channels are believed to be linear. For the AN data this is between 5 times its resolution and half its scale, and for the PC data this is below 15 MHz. The left panel of Fig. 1 shows one of such regressions, for a single profile and no delay. The right panel shows, for all 60 profiles, the R^2 coefficient from the fitting as a function of the time delay, from -10 up to 30 bins. The result indicates a time lag between 9 and 10 bins, i.e., of about 0.475 µs. For simplicity, all AN channels are corrected for a 10 bin delay (0.5 µs).

For extending the linear response of the PC channels above 15 MHz, the measured photon count readings are corrected for pulse pileup effects. For non-paralyzable systems (Whiteman et al., 1992; Knoll, 2010) the correction is

$$C(z,t,\tau) = N(z,t)/(1 - N(z,t)\tau),$$

where $N(z,t)$ and $C(z,t,\tau)$ are the uncorrected and corrected photon count rates, respectively, and τ is the dead time. The dead time is estimated as in Newsom et al. (2009) by varying τ during successive gluing procedures (Whiteman et al., 2006). In this procedure, because AN and corrected PC are linear, the true count rate is approximated by $\hat{C} = a\,\mathrm{AN} + b$, where $a(t)$ and $b(t)$ are the gluing coefficients, and τ is chosen to minimize the residual

$$J(t,\tau) = \frac{1}{n_j}\sum_z\left(\frac{C(z,t,\tau) - \hat{C}(z,t)}{\sigma_{ij}}\right)^2$$

for each profile at time t. Figure 2 shows an example $J(t,\tau)$ for τ between 1 and 7 ns. This was repeated for 580 one-min averaged nighttime profiles for the elastic and nitrogen Raman channels, and a histogram of the τ_{min} values are shown in Fig. 3. The found values, $\tau_{\mathrm{pmt\#1}} = 4.14 \pm 0.11$ ns and $\tau_{\mathrm{pmt\#2}} = 3.98 \pm 0.10$ ns, are in close agreement with manufacturer specification of 4 ns. Therefore, the default value is assumed to be correct for the photon count for the water vapor channel. Figure 4 shows a 20 min average PC example signal before and after the dead time correction. The dashed lines are the percentage difference to the glued signal, assumed to be the true count rate. The difference is negligible below 50 MHz. However, it reaches 5 % at only 125 MHz, showing that it is indeed necessary to combine the AN and PC data to increase the dynamical range of the detection system.

Electronic noise was evaluated by acquiring data during nighttime with the telescope covered. Figures 5 and 6 show the first 4000 bins for each of the five channels. The AN readings are all linear in the range of interest (< 30 km) for all 23 sample profiles with 100 shoots each. The photon count readings show very few random counts.

The system is fully automated and includes a clock-controlled external shutter to cover the telescope field of view from direct sunlight exposure between 11:00 a.m. and 02:00 p.m. local time (UTC – 3). As a backup system, a 10 mm shutter is positioned just above the iris and kept in its light-blocking position by a coil mechanism. Interlocks are connected to the power supply and to a light sensor inside a small telescope with a 10° field of view. The instrument itself is mounted within a special environmental cabinet, including an air conditioning and a dehumidifier, due to the harsh environment of Amazonia.

Good signal to noise ratio (S/N) is found above 15 km depending on the atmospheric conditions. The N_2 channel, 1 min average signals have good S/N up to 15 km but only during nighttime. For the H_2O channel, 1 min average signals have good S/N only up to 6 km during nighttime.

3 Analysis algorithm

3.1 Molecular reference

Rayleigh scattering by atmospheric molecules needs to be accurately estimated before the inversion of Lidar signals. The parameters characterizing this type of scattering are well documented in the literature (e.g. McCartney, 1976). The total cross section for Rayleigh scattering in a standard atmosphere is calculated as in Bucholtz (1995), i.e. without the approximation for the refractive index. This is, in turn, computed from the equations provided by Peck and Reeder (1972). The King correction factor for the depolarization of air molecules is computed separately for each constituent using the results from Bates (1984) and combined into a dry air factor following Bodhaine et al. (1999). The standard air CO_2 concentration is scaled to a constant value of 375 ppmv. The molecular scattering is hence computed as

$$\alpha_{\mathrm{m}}(\lambda,z) = N^{\mathrm{std}}\sigma_{\mathrm{m}}^{\mathrm{std}}(\lambda, 375\,\mathrm{ppmv\ CO_2})\frac{P(z)/T(z)}{P^{\mathrm{std}}/T^{\mathrm{std}}} \tag{1}$$

Radiosondes launched at 00:00 and 12:00 UTC from Ponta Pelada airport at 3.14° S 59.98° W, approximately 28.5 km south of the experimental Lidar site, were used to provide pressure and temperature profiles. Over a dense tropical rain forest one would

expect the thermodynamic profile to be horizontally homogeneous. The proximity of radiosonde site to Manaus city and the Amazon river requires, however, the verification of this hypothesis. Between 30 August and 5 September 2011, ten collocated soundings were launched during nighttime from the Lidar site and compared with the operational ones. Both sites used Vaisala RS92-SGP radiosondes. Figure 7 shows collocated minus operational profiles. The legend indicates the time difference in minutes between the two launches. Pressures and temperatures at the Lidar site are lower than those at the airport by about 5 hPa and 1 °C on average. For our purposes, however, the important result is that the air density, and hence the molecules number concentration, differ by less than 1 %.

The molecular backscatter coefficient is calculated from the molecular scattering and phase function considering the depolarization factor, ρ_{n}, as

$$\beta_{\mathrm{m}}(\lambda,z) = \frac{\alpha_{\mathrm{m}}(\lambda,z)}{4\pi}P_{\mathrm{ray}}(\pi,\lambda) = \frac{\alpha_{\mathrm{m}}(\lambda,z)}{8\pi/3}\frac{2}{2+\rho_{\mathrm{n}}} \tag{2}$$

which results in a molecular lidar ratio of $1.0153 \times 8\pi/3$ sr at 355 nm and $1.0150 \times 8\pi/3$ sr at 387 nm. The expected elastic return signal from a pure molecular atmosphere can then be calculated as

$$P_{\mathrm{m}}(\lambda_0,z) = K(\lambda_0)\frac{1}{z^2}\beta_{\mathrm{m}}(\lambda_0,z)\exp\left\{-2\int_0^z \alpha_{\mathrm{m}}(\lambda_0,z')\mathrm{d}z'\right\} \tag{3}$$

where the proportionality constant $K(\lambda_0)$ is determined by comparison of $P_{\mathrm{m}}(\lambda_0,z)$ with the background (BG) corrected elastic signal, $P(\lambda_0,z) - \mathrm{BG}$. Both $K(\lambda_0)$ and BG can be found by means of a simple linear regression,

$$P(\lambda_0,z) = K(\lambda_0)\cdot P_{\mathrm{m}}(\lambda_0,z) + \mathrm{BG}. \tag{4}$$

For the linear relation to hold, no aerosols can be present in the region selected for the regression. Therefore, only data above 8 km is used, as previous campaigns in the Amazon have shown that the aerosol concentration above this height is negligible (Baars, 2011). This, however, is verified in an interactive approach by calculating the distance between each point and the fitted curve,

$$\delta(z) = \frac{P(\lambda_0, z) - [K(\lambda_0) \cdot P_\mathrm{m}(\lambda_0, z) + \mathrm{BG}]}{\sqrt{\chi^2_\mathrm{red}}}, \tag{5}$$

where the reduced chi-square, χ^2_red, is used as a measure of the local noise level. Those points where $\delta(z) > 3$ or where the signal to noise ratio is $S/N < 15$ are removed. Both steps are repeated until no more points are excluded.

3.2 Aerosol inversions

During the day, the well-known Klett–Fernald (Klett, 1985; Fernald, 1984) method is used to solve the equation for the elastic Lidar return signal,

$$P(\lambda_0, z) = K(\lambda_0)\frac{O(z)}{z^2}\beta(\lambda_0, z)\exp\left\{-2\int_0^z \alpha(\lambda_0, z')\mathrm{d}z'\right\} \tag{6}$$

where $K(\lambda_0)$ includes all height-independent terms, $O(z)$ is the overlap function, $\beta = \beta_\mathrm{p} + \beta_\mathrm{m}$ is the total elastic backscatter coefficients and $\alpha = \alpha_\mathrm{p} + \alpha_\mathrm{m}$ is the total extinction coefficient. Assuming a height independent particle lidar ratio ($L_\mathrm{p} = \alpha_\mathrm{p}/\beta_\mathrm{p}$) and having chosen a reference height, z_0, where the particle contribution is negligible, i.e. $\beta_\mathrm{m}(z_0) \gg \beta_\mathrm{p}(z_0)$, the solution can be conveniently written as:

$$\beta_\mathrm{p}(z) = S(z)T(z, z_0)\left[\frac{S(z_0)}{\beta_\mathrm{m}(z_0)} - 2L_\mathrm{p}\int_{z_0}^{z} S(z')T(z', z_0)\mathrm{d}z'\right]^{-1} - \beta_\mathrm{m}(z) \tag{7}$$

$$T(z, z_0) = \exp\left[-2(L_\mathrm{p} - L_\mathrm{m})\int_{z_0}^{z} \beta_\mathrm{m}(r')\mathrm{d}r'\right] \tag{8}$$

where $S(z) = P(z)z^2$ is the range corrected signal and L_m is the molecular lidar ratio. The accuracy of this solution depends strongly on the molecular character of the reference value $S(z_0)$. This, however, is subject to noise fluctuations as the number of detected photons $P(z_0)$ has a Poisson distribution with $\lambda = \sqrt{P(z_0)}$. In some algorithms discussed in the literature (Fernald, 1984), a small but non-zero value of $\beta_p(z_0)$ is chosen to compensate the fact that $P(z_0) \neq P_m(z_0)$ at the starting point of the integration. There are also algorithms where the reference height is chosen to minimize $|P(z) - P_m(z)|$. Here the signal is assumed to be intrinsically noisy and an alternative approach is taken. If $P(z)$ has indeed a Poisson distribution around $P_m(z)$, the reference height is considered to be in the middle of the molecular region and $S(z_0) = S_m(z_0)$ is set.

During the night, the inversion method developed by Ansmann et al. (1992) is used to solve the equation for the nitrogen Raman return signal,

$$P(\lambda_\mathrm{R}, z) = K(\lambda_\mathrm{R})\frac{O(z)}{z^2}\beta(\lambda_\mathrm{R}, \lambda_0, z)\exp\left\{-\int_0^z \left[\alpha(\lambda_0, z') + \alpha(\lambda_\mathrm{R}, z')\right]\mathrm{d}z'\right\} \tag{9}$$

where the inelastic backscatter coefficient $\beta(\lambda_\mathrm{R}, \lambda_0, z) = N(z)\mathrm{d}\sigma(\lambda_\mathrm{R}, \lambda_0, \pi)/\mathrm{d}\Omega$ is given in terms of the number density of nitrogen molecules, N_R, and the differential cross section for the Raman inelastic scattering, $\mathrm{d}\sigma_\mathrm{R}/\mathrm{d}\Omega$. Assuming a wavelength dependence of λ^{-k} for both particles and molecules, the solution for the extinction coefficient is given by

$$\alpha_\mathrm{p}(\lambda_0, z) = \frac{\frac{\mathrm{d}}{\mathrm{d}z}\left\{\ln\left[\frac{N_\mathrm{R}(z)O(z)}{S_\mathrm{R}(z)}\right]\right\} - \alpha_\mathrm{m}(\lambda_0, z)\left[1 + (\lambda_0/\lambda_\mathrm{R})^{k_\mathrm{m}}\right]}{1 + (\lambda_0/\lambda_\mathrm{R})^{k_\mathrm{p}}} \tag{10}$$

where the overlap function was explicitly kept, S_R is the range corrected Raman signal and k_p and k_m are the angstrom coefficients for particles and molecules respectively. Having chosen a reference height z_0 where the particle contribution is negligible, the backscatter coefficient is given by

$$\beta_\mathrm{p}(\lambda_0,z) = -\beta_\mathrm{m}(\lambda_0,z) + \beta_\mathrm{m}(\lambda_0,z_0)\frac{S(z)/S_\mathrm{R}(z)}{S_\mathrm{m}(z_0)/S_\mathrm{m,R}(z_0)}\frac{N_\mathrm{R}(z)}{N_\mathrm{R}(z_0)} \times \exp\left\{\int\limits_{z_0}^{z}\left[\alpha(\lambda_0,z') - \alpha(\lambda_\mathrm{R},z')\right]\mathrm{d}z'\right\} \tag{11}$$

where $S(z_0)$ and $S_\mathrm{R}(z_0)$ were replaced by the calibrated molecular values $S_\mathrm{m}(z_0)$ and $S_\mathrm{m,R}(z_0)$ after the same arguments used for the Klett inversion. This solution is more stable than the one shown by Ansmann et al. (1992) as it does not depend at all on the noise fluctuations at z_0.

3.3 Overlap function

For a Lidar system with a narrow field of view and the usual separation between transmitter and receiver optical axes, an exact interpretation of Lidar return signal in the short range is complicated by the unknown factor of incomplete overlap between the transmitted laser beam and the telescope field of view. The methodology described by Wandinger and Ansman (2002) was used to obtain this factor.

All the data from July 2011 to November 2012 was divided into one-hour intervals and pre-processed to select the nighttime hours with no clouds or fog. About 90 one-hour averaged profiles were selected for the period before 1 August 2012, and 40 for the period after that. The distinction being the change of the field stop size from 4 mm (narrow) to 7 mm (wide), which increased the field of view of the telescope and hence lowered the maximum overlap. Figure 8 shows the results obtained from the application of the algorithm to each selected one-hour intervals. With the wide (narrow) field stop

the overlap is complete at about 1.8 km (3 km). Expanding the first term in Eq. (10), one find the contribution from the overlap function to the extinction coefficient in this lowermost part of the atmosphere (Baars, 2011):

$$\Delta\alpha_\mathrm{p}(\lambda_0,z) = \frac{\frac{\mathrm{d}}{\mathrm{d}z}[\ln O(z)]}{1+(\lambda_0/\lambda_\mathrm{R})^{k_\mathrm{p}}} \tag{12}$$

Figure 9 shows the average and 95 % confidence level limit of the overlap function in black, and the contribution to the extinction, from each individual one-hour period, in colors. For the cases after (before) the field stop change, the overlap correction is very important for altitudes below 1 km (1.5 km). It should be noted that, because Eq. (12) involves the derivative of $O(z)$ it stops giving an important contribution much before the altitude where $O(z) = 1$.

Another important point to consider regarding the overlap correction is the uncertainty in the values estimated by Eq. (12) that come from the difference between the average overlap and that of an individual measurement. As discussed by Baars (2011), this uncertainty can be estimated with the standard deviation of all contributions calculated with Eq. (12), i.e., the standard deviation of the colored lines shown in Fig. 9. This analysis is shown in Fig. 10. At 500 m, the error after (before) the field stop change is about 140 Mm^{-1} (480 Mm^{-1}).

3.4 Cloud base and top heights

The base and top heights of clouds are found using an algorithm similar to the one applied by Barja (2002). The algorithm uses only the signal and not its derivatives, as is usual in other methods appearing in the literature (e.g. Wang and Sassen, 2001). It is based on the fact that the intensity of the Lidar return signal in a pure molecular atmosphere decreases monotonically with increasing range and that an abrupt signal increment is found only when going trough a cloud layer. Therefore, the algorithm searches for a maximum in the signal and the corresponding previous minimum to determine the height of maximum backscattering and cloud base respectively. The cloud top is defined to be at the height at which the signal returns to behave as pure molecular. For thick clouds, where the signal is completed attenuated, an apparent cloud top is defined at the height at which the signal returns to the level it had at cloud base. Although the algorithm can be described in such simple terms, its implementation demands filters and statistical tests to remove the influence of noise, which are both system dependent. The algorithm steps are

1. compare the raw signal in each bin with its first neighbors and calculate all local minima and corresponding maxima;
2. apply a 3-point moving average to the raw signal and calculate all local minima and corresponding maxima of the filtered signal;
3. exclude those min/max pairs that are not found at the same time in the raw and filtered signals;
4. select min/max pairs corresponding to clouds by comparing the raw signal difference between maximum and minimum with the difference between raw and filtered signals at maximum;
5. select the cloud base height as the first minimum found when searching upwards and select the apparent cloud top height where the raw signal value is equal or less than signal value at cloud base;
6. find the height of maximum signal between base and top, i.e., the maximum backscattering height, and take note of the intermediary minima as they indicate sub-layers of the same cirrus cloud;
7. repeat steps 5–7 for the region above cloud top to identify other cirrus layers.

The pairs of base and top from the above steps are an approximation of the true base and top heights. They are used as a reference for the inversion algorithm to exclude the

cloudy part of the profile thus allowing for the calculation of the molecular and particle backscattering coefficients. The final base and top heights are defined as the heights where the particle backscattering coefficient is larger by two standard deviations than the average coefficient between 19 and 20 km as in Goldfarb et al. (2001).

4 Results and discussion

Results presented correspond to measurements taken from 30 August to 6 September 2011. Through this week an intensive campaign for calibration of the water vapor channel of the UV Raman Lidar was conducted. Besides having the thermodynamic profile from the collocated soundings, this period is also optimal because maintenance and verification were performed on a daily basis by an on site team and because of the low cloud cover typical of the Amazon dry season.

4.1 Vertical profiles of aerosols

The aerosol backscatter coefficient was obtained from the elastic channels using Eqs. (7) and (8) with a lidar ratio of 55 sr, which is typical for aged biomass burning aerosols found in this region during the transition from the dry to wet seasons (Baars et al., 2012). This is shown in Fig. 11 where the grayed regions correspond to local solar noon when the instrument was not operated. Other data not shown corresponds to cloud, precipitation or fog events that can be identified in the range corrected signal (upper panel). Values exceeding 3 $\mathrm{Mm^{-1}\,sr^{-1}}$ were found. In the lower panel of Fig. 11 the extinction coefficient for the chosen lidar ratio is shown. Maximum aerosol extinction varies from 70 to 160 $\mathrm{Mm^{-1}}$. There were events where the aerosol was washed out after precipitation and extinction was reduced significantly (e.g. 30 August 02:00 p.m.) but events where the aerosol loading remained the same were much more often (e.g. 31 August 02:00 p.m., 1 September 06:00 a.m., 2 September 03:00 p.m. and 3 September 07:00 a.m.).

Figure 12 shows the backscatter (top) and extinction (middle) coefficients calculated independently with the Raman algorithm during nighttime (18:30 to 05:50 LT). An angstrom coefficient of 1.2 was used as an average value for August–October in this region, obtained from AERONET measurements (Schafer et al., 2008) and a 5 min running average was applied. Aerosol plumes with backscatter coefficient above 3 $\mathrm{Mm^{-1}\,sr^{-1}}$ were also seen on 1 and 2 September and an aerosol layer between 1 and 2.5 km can be identified. This elevated layer appears at heights typical of biomass burning plumes transported over long distances, as characterized by previous Lidar studies in the region (Baars et al., 2012). Extinction coefficients from the Raman algorithm (Fig. 12 middle panel) are much more noisy than the elastic inversion as expected, owing to the derivative in Eq. (10). Largest values were around 150 $\mathrm{Mm^{-1}}$ inside the plume, about the same as found above. Extinction coefficients close to ground level (at about 750 m) ranged from 40 to 100 $\mathrm{Mm^{-1}}$ at 355 nm, which is compatible with the values measured at ground level by Artaxo et al. (2013) during the dry season (10–40 $\mathrm{Mm^{-1}}$ at 670 nm). The last panel in Fig. 12 shows the lidar ratio computed from the Raman coefficients for extinction and backscatter larger than 5 $\mathrm{Mm^{-1}}$ and 0.05 $\mathrm{Mm^{-1}\,sr^{-1}}$ respectively. Values were about 45 to 70 sr compatible with what is expected for biomass burning aerosols and explaining why the elastic inversion with fixed lidar ratio of 55 sr showed good results.

4.2 Aerosol optical depth

The aerosol optical depth can be obtained from the light extinction by vertically integrating each profile. However, as the partial overlap significantly impacts the extinction below 1.2 km (Fig. 9), integrating over this region could lead to unrealistic results. Therefore, we assumed a well-mixed boundary layer with a constant extinction up to 1.2 km, which will be justified below, and calculated the column AOD from all the 1 min profiles of the Klett and Raman extinction coefficients. Figure 13 shows a scatter plot of the elastic AOD vs. the Raman AOD for 4435 nighttime profiles. There is a very good agreement and the linear and angular coefficients are statistically significant at

95 % confidence level to be compatible with 0 and 1 respectively. As the elastic AOD is similar to the Raman AOD, we used the profiles measured during daytime to validate our Lidar measurements against the collocated AERONET station. The AERONET AOD at 355 nm was estimated from that at 340 nm using the angstrom coefficient between 340–380 nm. A good agreement was found, as shown in Fig. 14, and AERONET measurement around local noon nicely matches the Lidar data before and after this period. Remotely sensed aerosol optical depth measurements at 550 nm were taken from the MODIS (The MODerate resolution Imaging Spectroradiometer Remer et al., 2005) Atmosphere Products, MOD04L2 and MYD04L2, Collection 5. MODIS AOD was averaged in an area of 40 km × 40 km around the site and scaled to 355 nm using an averaged angstrom coefficient of 1.11 between 380–500 nm estimated by AERONET. MODIS-Aqua agrees with both AERONET and Lidar measurements, while MODIS-Terra do not. Very few points are available, however, and no definitive conclusion can be drawn from this comparison.

For a quantitative validation, the Lidar data were averaged in time around each AERONET measurement and compared one by one. As the averaging time window and the height of the constant extinction near ground are somewhat arbitrary, the ranges of possible values were explored for determining the best choice. The time window width was varied from 1 to 60 min, while the altitude of the layer with constant extinction was varied from 0.5 to 2 km. Left panel of Fig. 15 shows the correlation between the time series of AERONET and Lidar AOD's as a function of these two parameters. Highest values are found around 1.25 and 1.6 km. A high correlation value, however, does not mean that AERONET and Lidar values are close, hence the root mean square error was calculated and is shown in the right panel. The minimum error is found when assuming a constant extinction below 1.3 km and doing a 30 min time average, in good agreement with our previous choice of 1.2 km based on the overlap uncertainty. Having defined the best parameters, a comparison of the AERONET AOD and the elastic Lidar AOD was performed and is shown in Fig. 16. The angular coefficient is compatible with 1 and RMSE is only 0.06, comparable to the AERONET AOD uncertainty.

4.3 Back trajectories

For identifying the source of aerosol particles observed during this week, backward trajectories from the Hysplit model (Draxler and Hess, 1998) and fire spots identified by the *Instituto Nacional de Pesquisas Espaciais (INPE)* using a combination of satellites[1] were used. As the largest AOD values (~ 0.7) were measured on 3 September (Fig. 16), back trajectories were started at 12:00 UTC of that day from the height of maximum extinction (~ 1.5 km, see Fig. 12). Hysplit was run in ensemble mode, by shifting the starting point by one model grid box up/down, east/west and north/south. These 27 different trajectories are shown in Fig. 17 with all fire spots observed between 30 August to 1 September. Some trajectories could carry biomass burning aerosol as they cross nearby fire spots in West Para and more distant ones in East Para and Maranhão. Other trajectories, however, come straight from the ocean and should bring clean air. Local sources of fires could also contribute. The dilution of the polluted air masses could explain the large variations observed in AOD during this week, from below 0.05 up to 0.75, with a rather constant lidar ratio (Fig. 12).

4.4 High clouds geometrical characteristics

Figure 18 shows the logarithm of range and background corrected signal at 355 nm for altitudes above 5 km during the intensive campaign. As in the previous results, lacking measurements around local solar noon is due to the high sun elevation. Other missing data at these altitudes are produced by the low clouds that attenuate the beam at lower levels. The presence of high clouds is easily depicted by the highest values in the signal, shown in red. These high clouds are very frequent and appear at altitudes from 6 km to 20 km, with higher activity after the first two days.

---

[1] http://www.inpe.br/queimadas/

The high cloud base and top heights found by our automatic algorithm, and the −25 °C and tropopause heights from the radiosondes are shown in the same figure. There is a good agreement between these geometrical characteristics indicating that the algorithm has an overall good performance. However, there are also some base and top heights detected that have no correspondence in the raw signal, for instance, at 5 September 2011 between 09:00 and 10:00 LT. The explanation is that while the background corrected signal is shown only for values above three standard deviations above the background, the high cloud algorithm processes the raw signal. The base and top altitudes found at this period are similar to those found before and after, hence indicating a single high cloud layer. This means that the algorithm has discrimination power even at S/N below 3.

In Fig. 18 there are persistent high clouds from the third to the last day of measurement. The bases and tops are in the range expected for tropical latitudes cirrus (e.g. Immler and Schrems, 2002), with top heights around 15 km or higher and base heights around 9 km or higher. These tropical tropopause cirrus clouds may have originated from deep convection in the region, as 5 deep convection events with rain rates between 25 and 222 mm hr^{-1} were measured by the collocated weather station. The accumulated precipitation in 1, 3 and 5 September, was 9.35, 28.68 and 17.51 mm. The total precipitation during the intensive campaign was 57.79 mm, half of that accumulated in September (113.5 mm). It is also interesting to note the presence of very optically thick clouds as high as 8–12 km. These seem to be the stratiform part of convective towers as they are found at increasingly higher altitudes (e.g., 1, 3, 5 and 6 September). At 15:00 LT these clouds are around 6–8 km and at 18:00–21:00 LT they are at the tropopause, thus in agreement with the diurnal cycle of local convection in the Amazon (e.g. Machado et al., 2002). This is a strong indication that these cirrus clouds are produced by deep convection, but further analysis with satellite images and back trajectories will be performed in a upcoming study.

Table 1 summarizes the cloud measurements. During the whole period the mean value of base, top and maximum backscattering heights were 11.5 km, 13.4 km and

12.8 km, respectively. The maximum/minimum values for these characteristics during overall period were 17.9 km/6.0 km, 19.5 km/6.5 km and 19.2 km/6.4 km, respectively. On average, the maximum backscattering heights are closer to the top altitude. From the algorithm, it was also obtained the multiple layers of clouds and the sub layers structure inside these high clouds. Up to 3 high clouds layers were detected during almost overall period. Only the first two days have 1 or 2 layers and also correspond to the lowest high cloud frequency occurrence, with only 3 % and 15 % respectively.

5 Conclusions

This paper described a permanent UV Raman Lidar station, which become fully operational in central Amazon in July 2011. The system was designed for unattended, continuous measurements of aerosols and water vapor aiming to study and monitor the atmosphere on the weather to climatic time scales. The automated data acquisition and the possibility to monitor the instrument over the internet reduced the operational field costs of maintaining on-site personnel and enabled extended hours of daily data collection when compared to a manually operated systems. This new scientific facility has the potential to significantly improve the knowledge of the aerosol vertical distribution over Amazonia that, until now, has been based on about a handful of short-period intensive campaigns.

The instrument was thoroughly described and characterized. The delay of the analog and the dead time of the photon count channels were obtained experimentally. In the first case, a 0.475 µs was found corresponding to a 10-bin displacement. For the pulse pile up effects, a dead time 4.14 (11),ns and 3.98 (10) ns were measured for the first two channels, in agreement with the manufacturer specification. Therefore, the analysis algorithm automatically desaturates the three photon count channels assuming a non-paralyzable system with $\tau = 4$ ns, and correct the analog channels for the time delay. The overlap between the laser beam and the telescope field of view was experimentally determined using the method of Wandinger and Ansman (2002). For the period before

1 August 2012, when the system used a narrow field stop, a full overlap was found at 3 km and its contribution to the particle extinction was found to be important below 1.5 km. For the period with the wide field stop, these were 1.8 km and 1 km respectively. Widening the field stop allowed reducing the overlap correction uncertainty to the extinction coefficient from 88 to 36 $\text{Mm}^{-1}\,\text{sr}^{-1}$ at 750 m. Ten radiosondes were launched from the Lidar site and compared to simultaneous measurements at the operational sounding site at the Manaus military airport. Differences in molecules number concentration were found to be less than 1 %, hence the operational soundings are used for our routine analysis.

A week of Lidar measurements during the biomass burning season of 2011 were analyzed and compared with measurements from a co-located AERONET sun photometer as a mean to assess the overall system capability and performance. The period chosen was from 30 August to 6 September 2011 when an intensive campaign for calibration of the water vapor channel of the UV Raman Lidar was conducted (to be discussed in an upcoming publication). Lidar ratios obtained during nighttime with the use of the Raman channel were between 50 and 65 sr during the whole week, compatible with values found by previous measurements of biomass burning aerosols in the region (Baars et al., 2012). A comparison of the elastic (LR = 55 sr) and raman aerosol optical depth for each 1 min cloud-free night-time profile during that week showed no systematic differences, thus allowing us to use the elastic method to compare Lidar and AERONET measurements during day time. Lidar data was averaged in a 30 min window around the AERONET measurements, and again no systematic differences were found. The RMSE for the AOD was 0.06 with a $R^2 = 0.75$, small compared to range of observed AOD values 0.1 to 0.75 and to the total AERONET uncertainty that is about 0.02 (Holben et al., 1998). To identify the source of these particles, a backtrajectory analysis was performed using the Hysplit model from NOAA and fire detection maps from INPE. An ensemble of backtrajectories shows about half coming from the ocean and half from the fire spots region. We therefore concluded that these particles were originated from biomass burning. Moreover, as the measured lidar ratio was rather constant even for low aerosol loadings, we also concluded that the mixture of clean air into the polluted air masses diluted the smoke plumes, therefore explaining the alternation of low (~ 0.1) and high (~ 0.7) AOD values with constant LR.

A cloud detection algorithm initially developed by Barja (2002) was improved and applied to data from that same week to detect cirrus clouds. A visual inspection of the range corrected signal and the algorithm output for the cloud base, top and height of maximum backscatter shows a very good agreement. During this period, cirrus clouds were present in 60 % of our measurements in agreement with previous results (Wang and Sassen, 2001), but with high day to day variability (occurrence frequency varied from 15 to 83 %). Average base and top heights were 11.5 and 13.4 km respectively, and maximum backscatter at 12.8 km. Most of the time, three layers of cirrus clouds were found.

Acknowledgements. We would like to acknowledge the financial support from FAPESP Research Program on Global Climate Change under research grants 2008/58100-1, 2009/15235-8, 2011/50170-4, 2012/14437-9 and 2012/16100-1. We were also supported by the Instituto Nacional de Ciência e Tecnologia (INCT) – Mudanças Climáticas and CNPq grants 477575/2008-0, 475735/2012-9 and 457843/2013-6. We are grateful to Mr. Fernando Morais for operation of the AERONET station at Manaus. We thank Alcides C. Ribeiro, Ana L. Loureiro, Fábio de Oliveira Jorge and Simara Morais for technical and logistical support. Operation of the instruments at the experimental site would not have been possible without the institutional support from EMBRAPA and INPA (Instituto Nacional de Pesquisas da Amazonia) LBA Central Office in Manaus. Special thanks to Marcelo Rossi, Victor Souza and Jocivaldo Souza at Embrapa, and to Ruth Araújo and Roberta Souza from INPA-LBA.

References

Adams, D. K., Fernandes, R. M. S., Kursinski, E. R., Maia, J. M., Sapucci, L. F., Machado, L. A. T., Vitorello, I., Monico, J. F. G., Holub, K. L., Gutman, S. I., Filizola, N., and Bennett, R. A.: A dense GNSS meteorological network for observing deep convection in the Amazon, Atmos. Sci. Lett., 12, 207–212, doi:10.1002/asl.312, 2011. 774

Andreae, M. O., Browell, E. V., Garstang, M., Gregory, G. L., Harriss, R. C., Hill, G. F., Jacob, D. J., Pereira, M. C., Sachse, G. W., Setzer, A. W., Dias, P. L. S., Talbot, R. W., Torres, A. L., and Wofsy, S. C.: Biomass-burning emissions and associated haze layers over Amazonia, J. Geophys. Res., 93, 1509–1527, doi:10.1029/JD093iD02p01509, 1988. 771

Andreae, M. O., Artaxo, P., Fischer, H., Freitas, S. R., Grégoire, J.-M., Hansel, A., Hoor, P., Kormann, R., Krejci, R., Lange, L., Lelieveld, J., Lindinger, W., Longo, K., Peters, W., de Reus, M., Scheeren, B., Silva Dias, M. A. F., Ström, J., van Velthoven, P. F. J., and Williams, J.: Transport of biomass burning smoke to the upper troposphere by deep convection in the equatorial region, Geophys. Res. Lett., 28, 951–954, doi:10.1029/2000GL012391, 2001. 772

Andreae, M. O., Rosenfeld, D., P., A., Costa, A. A., Frank, G. P., Longo, K. M., and Silva-Dias, M. A. F.: Smoking rain clouds over the Amazon, Science, 303, 1337–1342, 2004. 771

Ansmann, A., Wandinger, U., Riebesell, M., Weitkamp, C., and Michaelis, W.: Independent measurement of extinction and backscatter profiles in cirrus clouds by using a combined Raman elastic-backscatter lidar, Appl. Optics, 31, 7113–7131, 1992. 780, 781

Artaxo, P., Rizzo, L. V., Brito, J. F., Barbosa, H. M. J., Arana, A., Sena, E. T., Cirino, G. G., Bastos, W., Martin, S. T., and Andreae, M. O.: Atmospheric aerosols in Amazonia and land use change: from natural biogenic to biomass burning conditions, Faraday Discuss., 165, 203–235, doi:10.1039/C3FD00052D, 2013. 771, 774, 785

Baars, H.: Aerosol profiling with lidar in the Amazon Basin during the wet and dry season 2008, Ph.D. thesis, IfT, Leipzig, 191 pp., 2011. 772, 779, 782

Baars, H., Ansmann, A., Althausen, D., Engelmann, R., Artaxo, P., Pauliquevis, T., and Souza, R.: Further evidence for significant smoke transport from Africa to Amazonia, Geophys. Res. Lett., 38, L20802, doi:10.1029/2011GL049200, 2011. 772

Baars, H., Ansmann, A., Althausen, D., Engelmann, R., Heese, B., Müller, D., Artaxo, P., Paixao, M., Pauliquevis, T., and Souza, R.: Aerosol profiling with lidar in the Amazon Basin during the wet and dry season, J. Geophys. Res., 117, D21201, doi:10.1029/2012JD018338, 2012. 773, 784, 785, 790

Barja, B.: Tropical Cirrus Clouds Measurements at camagüey, Cuba, in: Lidar Remote Sensing in Atmospheric and Earth Sciences, Part II, edited by: Bissonnette, L., Roy, G. and Valle, G., 21st International Laser Radar Conference, 673–675, 2002. 782, 791

Bates, D. R.: Rayleigh scattering by air, Planet. Space Sci., 32, 785–790, 1984. 777

Bevan, S. L., North, P. R. J., Grey, W. M. F., Los, S. O., and Plummer, S. E.: Impact of atmospheric aerosol from biomass burning on Amazon dry-season drought, J. Geophys. Res., 114, D09204, doi:10.1029/2008JD011112, 2009. 771

Bodhaine, B. A., Wood, N. B., Dutton, E. G., and Slusser, J. R.: On rayleigh optical depth calculations, J. Atmos. Ocean. Tech., 16, 1854, doi:10.1175/1520-0426(1999)016<1854:ORODC>2.0.CO;2, 1999. 777

Boucher, O., Randall, D., Artaxo, P., Bretherton, C., Feingold, G., Forster, P., Kerminen, V.-M., Kondo, Y., Liao, H., Lohmann, U., Rasch, P., Satheesh, S. K., Sherwood, S., Stevens, B., and Zhang, X. Y.: Clouds and aerosols, in: Climate Change 2013: The Physical Science Basis. Contribution of Working Group I to the Fifth Assessment Report of the Intergovernmental Panel on Climate Change, Cambridge University Press, Cambridge, UK, New York, NY, USA, 2013. 773

Bucholtz, A.: Rayleigh-scattering calculations for the terrestrial atmosphere, Appl. Optics, 34, 2765–2773, 1995. 777

Butt, N., de Oliveira, P. A., and Costa, M. H.: Evidence that deforestation affects the onset of the rainy season in Rondonia, J. Geophys. Res., 116, 2–9, doi:10.1029/2010JD015174, 2011. 771

Chand, D., Guyon, P., Artaxo, P., Schmid, O., Frank, G. P., Rizzo, L. V., Mayol-Bracero, O. L., Gatti, L. V., and Andreae, M. O.: Optical and physical properties of aerosols in the boundary layer and free troposphere over the Amazon Basin during the biomass burning season, Atmos. Chem. Phys., 6, 2911–2925, doi:10.5194/acp-6-2911-2006, 2006. 772

Cirino, G. G., Souza, R. F., Adams, D. K., and Artaxo, P.: The effect of atmospheric aerosol particles and clouds on Net Ecosystem Exchange in Amazonia, Atmos. Chem. Phys. Discuss., 13, 28819–28868, doi:10.5194/acpd-13-28819-2013, 2013. 771

Davidson, E. A. and Artaxo, P.: Globally significant changes in biological processes of the Amazon Basin: results of the large-scale biosphere–atmosphere experiment, Glob. Change Biol., 10, 519–529, doi:10.1111/j.1529-8817.2003.00779.x, 2004. 770

Draxler, R. and Hess, G.: An overview of the HYSPLIT 4 modeling system of trajectories, dispersion, and deposition, Aust. Meteorol. Mag., 47, 295–308, 1998. 787

Feingold, G.: First measurements of the Twomey indirect effect using ground-based remote sensors, Geophys. Res. Lett., 30, 1287, doi:10.1029/2002GL016633, 2003. 771

Fernald, F. G.: Analysis of atmospheric lidar observations: some comments, Appl. Optics, 23, 652–653, 1984. 779, 780

Formenti, P., Andreae, M. O., Lange, L., Roberts, G., Cafmeyer, J., Rajta, I., Maenhaut, W., Holben, B. N., Artaxo, P., and Lelieveld, J.: Saharan dust in Brazil and Suriname during the Large-scale Biosphere–Atmosphere experiment in Amazonia (LBA) – Cooperative LBA Regional Experiment (CLAIRE) in March 1998, J. Geophys. Res., 106, 14919–14934, doi:10.1029/2000JD900827, 2001. 772, 773

Forster, P., Ramaswamy, V., Artaxo, P., Berntsen, T., Betts, R., Fahey, D., Haywood, J., Lean, J., Lowe, D., Myhre, G., Nganga, J., Prinn, R., Raga, G., Schulz, M., and Van Dorland, R.: Changes in atmospheric constituents and in radiative forcing, in: Climate Change 2007: The Physical Science Basis. Contribution of Working Group I to the Fourth Assessment Report of the Intergovernmental Panel on Climate Change, Cambridge University Press, Cambridge, UK, New York, NY, USA, 2007. 771

Freud, E., Rosenfeld, D., Andreae, M. O., Costa, A. A., and Artaxo, P.: Robust relations between CCN and the vertical evolution of cloud drop size distribution in deep convective clouds, Atmos. Chem. Phys., 8, 1661–1675, doi:10.5194/acp-8-1661-2008, 2008. 771

Goldfarb, L., Keckhut, P., Chanin, M.-L., and Hauchecorne, A.: Cirrus climatological results from lidar measurements at OHP (44° N. 6° E), Geophys. Res. Lett., 28, 1687–1690, 2001. 784

Guyon, P., Frank, G. P., Welling, M., Chand, D., Artaxo, P., Rizzo, L., Nishioka, G., Kolle, O., Fritsch, H., Silva Dias, M. A. F, Gatti, L. V., Cordova, A. M., and Andreae, M. O.: Airborne measurements of trace gas and aerosol particle emissions from biomass burning in Amazonia, Atmos. Chem. Phys., 5, 2989–3002, doi:10.5194/acp-5-2989-2005, 2005. 772

Harriss, R. C., Wofsy, S. C., Garstang, M., Browell, E. V., Molion, L. C. B., McNeal, R. J., Hoell, J. M., Bendura, R. J., Beck, S. M., Navarro, R. L., Riley, J. T., and Snell, R. L.: The Amazon Boundary Layer Experiment (ABLE 2A): dry season 1985, J. Geophys. Res., 93, 1351–1360, doi:10.1029/JD093iD02p01351, 1988. 771

Holben, B., Eck, T., Slutsker, I., Tanré, D., Buis, J., Setzer, A., Vermote, E., Reagan, J., Kaufman, Y., Nakajima, T., Lavenu, F., Jankowiak, I., and Smirnov, A.: AERONET – a federated instrument network and data archive for aerosol characterization, Remote Sens. Environ., 66, 1–16, doi:10.1016/S0034-4257(98)00031-5, 1998. 774, 790

Immler, F. and Schrems, O.: Determination of tropical cirrus properties by simultaneous lidar and radiosondemeasurements, Geophys. Res. Lett., 29, 2090, doi:10.1029/2002GL015076, 2002. 788

Kaufman, Y. J., Hobbs, P. V., Kirchhoff, V. W. J. H., Artaxo, P., Remer, L. A., Holben, B. N., King, M. D., Ward, D. E., Prins, E. M., Longo, K. M., Mattos, L. F., Nobre, C. A., Spinhirne, J. D., Ji, Q., Thompson, A. M., Gleason, J. F., Christopher, S. A., and Tsay, S.-C.: Smoke, Clouds, and Radiation-Brazil (SCAR-B) experiment, J. Geophys. Res., 103, 31783–31808, doi:10.1029/98JD02281, 1998. 771

Kaufman, Y. J., Koren, I., Remer, L. A., Tanré, D., Ginoux, P., and Fan, S.: Dust transport and deposition observed from the Terra-Moderate Resolution Imaging Spectroradiometer (MODIS) spacecraft over the Atlantic Ocean, J. Geophys. Res., 110, D10S12, doi:10.1029/2003JD004436, 2005. 773

Klett, J. D.: Lidar inversion with variable backscatter/extinction ratios, Appl. Optics, 24, 1638–1643, 1985. 779

Knoll, G. F.: Radiation Detection and Measurement, John Wiley & Sons, Inc., United State of America, 25, 4th Edn., 830 pp., 2010. 775

Koren, I., Altaratz, O., Remer, L. A., Feingold, G., Martins, J. V., and Heiblum, R. H.: Aerosol-induced intensification of rain from the tropics to mid-latitudes, Nat. Geosci., 5, 118–122, doi:10.1038/ngeo1364, 2012. 771

Krejci, R., Ström, J., de Reus, M., Hoor, P., Williams, J., Fischer, H., and Hansson, H.-C.: Evolution of aerosol properties over the rain forest in Surinam, South America, observed from aircraft during the LBA-CLAIRE 98 experiment, J. Geophys. Res., 108, 4561, doi:10.1029/2001JD001375, 2003. 772

Kuhn, U., Ganzeveld, L., Thielmann, A., Dindorf, T., Schebeske, G., Welling, M., Sciare, J., Roberts, G., Meixner, F. X., Kesselmeier, J., Lelieveld, J., Kolle, O., Ciccioli, P., Lloyd, J., Trentmann, J., Artaxo, P., and Andreae, M. O.: Impact of Manaus City on the Amazon Green Ocean atmosphere: ozone production, precursor sensitivity and aerosol load, Atmos. Chem. Phys., 10, 9251–9282, doi:10.5194/acp-10-9251-2010, 2010. 771

Kulmala, M., Asmi, A., Lappalainen, H. K., Baltensperger, U., Brenguier, J.-L., Facchini, M. C., Hansson, H.-C., Hov, Ø., O'Dowd, C. D., Pöschl, U., Wiedensohler, A., Boers, R., Boucher, O., de Leeuw, G., Denier van der Gon, H. A. C., Feichter, J., Krejci, R., Laj, P.,

Lihavainen, H., Lohmann, U., McFiggans, G., Mentel, T., Pilinis, C., Riipinen, I., Schulz, M., Stohl, A., Swietlicki, E., Vignati, E., Alves, C., Amann, M., Ammann, M., Arabas, S., Artaxo, P., Baars, H., Beddows, D. C. S., Bergström, R., Beukes, J. P., Bilde, M., Burkhart, J. F., Canonaco, F., Clegg, S. L., Coe, H., Crumeyrolle, S., D'Anna, B., Decesari, S., Gilardoni, S., Fischer, M., Fjaeraa, A. M., Fountoukis, C., George, C., Gomes, L., Halloran, P., Hamburger, T., Harrison, R. M., Herrmann, H., Hoffmann, T., Hoose, C., Hu, M., Hyvärinen, A., Hõrrak, U., Iinuma, Y., Iversen, T., Josipovic, M., Kanakidou, M., Kiendler-Scharr, A., Kirkevåg, A., Kiss, G., Klimont, Z., Kolmonen, P., Komppula, M., Kristjánsson, J.-E., Laakso, L., Laaksonen, A., Labonnote, L., Lanz, V. A., Lehtinen, K. E. J., Rizzo, L. V., Makkonen, R., Manninen, H. E., McMeeking, G., Merikanto, J., Minikin, A., Mirme, S., Morgan, W. T., Nemitz, E., O'Donnell, D., Panwar, T. S., Pawlowska, H., Petzold, A., Pienaar, J. J., Pio, C., Plass-Duelmer, C., Prévôt, A. S. H., Pryor, S., Reddington, C. L., Roberts, G., Rosenfeld, D., Schwarz, J., Seland, Ø., Sellegri, K., Shen, X. J., Shiraiwa, M., Siebert, H., Sierau, B., Simpson, D., Sun, J. Y., Topping, D., Tunved, P., Vaattovaara, P., Vakkari, V., Veefkind, J. P., Visschedijk, A., Vuollekoski, H., Vuolo, R., Wehner, B., Wildt, J., Woodward, S., Worsnop, D. R., van Zadelhoff, G.-J., Zardini, A. A., Zhang, K., van Zyl, P. G., Kerminen, V.-M., S Carslaw, K., and Pandis, S. N.: General overview: European Integrated project on Aerosol Cloud Climate and Air Quality interactions (EUCAARI) – integrating aerosol research from nano to global scales, Atmos. Chem. Phys., 11, 13061–13143, doi:10.5194/acp-11-13061-2011, 2011. 772

Machado, L. A. T., Laurent, H., and Lima, A. A.: Diurnal march of the convection observed during TRMM-WETAMC/LBA, J. Geophys. Res., 107, 8064, doi:10.1029/2001JD000338, 2002. 788

Machado, L. A. T., Dias, M. A. F. S., Morales, C., Fisch, G., Vila, D., Albrecht, R., Goodman, S. J., Calheiros, A., Biscaro, T., Kummerow, C., Cohen, J., Fitzjarrald, D., Nascimento, E., Sakamoto, M., Cunningham, C., Chaboureau, J.-P., Petersen, W. A., Adams, D., Baldini, L., Angelis, C. F., Sapucci, L. F., Salio, P., Barbosa, H. M. J., Landulfo, E., Souza, R. F., Blakeslee, R. J., Bailey, J., Freitas, S., Lima, W. F. A., and Tokay, A.: The CHUVA Project – how does convection vary across the Brazil?, B. Am. Meteorol. Soc., submitted, 2014. 774

Martin, S. T., Andreae, M. O., Althausen, D., Artaxo, P., Baars, H., Borrmann, S., Chen, Q., Farmer, D. K., Guenther, A., Gunthe, S. S., Jimenez, J. L., Karl, T., Longo, K., Manzi, A., Müller, T., Pauliquevis, T., Petters, M. D., Prenni, A. J., Pöschl, U., Rizzo, L. V., Schneider, J., Smith, J. N., Swietlicki, E., Tota, J., Wang, J., Wiedensohler, A., and Zorn, S. R.: An overview of the Amazonian Aerosol Characterization Experiment 2008 (AMAZE-08), Atmos. Chem. Phys., 10, 11415–11438, doi:10.5194/acp-10-11415-2010, 2010. 772

McCartney, E. J.: Optics of the Atmosphere: Scattering by Molecules and Particles, John Wiley, New York, 1976. 777

Newsom, R. K., Turner, D. D., Mielke, B., Clayton, M. F., Ferrare, R., and Sivaraman, C.: Simultaneous analog and photon counting detection for Raman lidar, Appl. Optics, 48, 3903–3914, 2009. 776

Oliveira, P. H. F., Artaxo, P., Pires, C., de Lucca, S., Procópio, A., Holben, B., Schafer, J., Cardoso, L. F., Wofsy, S. C., and Rocha, H. R.: The effects of biomass burning aerosols and clouds on the CO_2 flux in Amazonia, Tellus B, 59, 338–349, doi:10.1111/j.1600-0889.2007.00270.x, 2007. 771

Pauliquevis, T., Barbosa, H. M. J., et al.: The Aerosols Clouds-cONVection EXperiment (ACONVEX), in preparation, 2014. 774

Peck, E. R. and Reeder, K.: Dispersion of air, J. Opt. Soc. Am., 62, 958–962, 1972. 777

Pereira, E. B., Setzer, A. W., Gerab, F., Artaxo, P. E., Pereira, M. C., and Monroe, G.: Airborne measurements of aerosols from burning biomass in Brazil related to the TRACE A experiment, J. Geophys. Res., 101, 23983–23992, doi:10.1029/96JD00098, 1996. 772

Reid, J. S., Hobbs, P. V., Ferek, R. J., Blake, D. R., Martins, J. V., Dunlap, M. R., and Liousse, C.: Physical, chemical, and optical properties of regional hazes dominated by smoke in Brazil, J. Geophys. Res., 103, 32059–32080, doi:10.1029/98JD00458, 1998. 771

Remer, L. A., Kaufman, Y. J., Tanré, D., Mattoo, S., Chu, D. A., Martins, J. V., Li, R.-R., Ichoku, C., Levy, R. C., Kleidman, R. G., Eck, T. F., Vermote, E., and Holben, B. N.: The MODIS aerosol algorithm, products, and validation, J. Atmos. Sci., 62, 947–973, doi:10.1175/JAS3385.1, 2005. 786

Schafer, J. S., Eck, T. F., Holben, B. N., Artaxo, P., and Duarte, A. F.: Characterization of the optical properties of atmospheric aerosols in Amazônia from long-term AERONET monitoring (1993–1995 and 1999–2006), J. Geophys. Res., 113, 1–16, doi:10.1029/2007JD009319, 2008. 785

Talbot, R. W., Andreae, M. O., Berresheim, H., Artaxo, P., Garstang, M., Harriss, R. C., Beecher, K. M., and Li, S. M.: Aerosol chemistry during the wet season in central Amazonia: the influence of long-range transport, J. Geophys. Res., 95, 16955–16969, doi:10.1029/JD095iD10p16955, 1990. 773

Wandinger, U. and Ansman, A.: Experimental determination of the lidar overlap profile with Raman lidar, Appl. Optics, 41, 511–514, 2002. 781, 789

Wang, Z. and Sassen, K.: Cloud type and macrophysical property retrieval using multiple remote sensors, J. Appl. Meteorol., 40, 1665–1682, 2001. 782, 791

Whiteman, D. N., Melfi, S. H., and Ferrare, R. A.: Raman lidar system for measurement of water vapor and aerosols in the Earth's atmosphere, Appl. Optics, 31, 3068–3082, 1992. 775

Whiteman, D. N., Demoz, B., Rush, K., Schwemmer, G., Gentry, B., Di Girolamo, P., Comer, J., Veselovskii, I., Evans, K., Melfi, S. H., Wang, Z., Cadirola, M., Mielke, B., Venable, D., and Van Hove, T.: Raman lidar measurements during the international H_2O Project – Part 1: Instrumentation and analysis techniques, J. Atmos. Ocean. Tech., 23, 157–169, doi:10.1175/JTECH1838.1, 2006. 776

Table 1. Average geometrical characteristics (base, top and maximum backscattering height) and frequency of occurrence of cirrus clouds in the measurement site near Manaus city during 30 August and 7 September 2011.

	ALL	8/30	8/31	9/1	9/2	9/3	9/4	9/5	9/6	9/7
#cirrus clouds detected	983	8	36	160	146	198	92	157	116	70
Occurrence Frequency (%)	60	3	15	70	61	83	59	67	53	60
Quantity of cirrus layer		2	1	3	3	3	3	3	3	3
Base (km)	11.5	12.0	13.9	12.6	12.5	10.9	11.4	10.7	11.3	10.2
Top (km)	13.4	12.6	14.5	14.2	14.0	13.0	13.9	12.7	13.5	12.4
Max. back. (km)	12.8	12.4	14.2	13.6	13.5	12.2	13.0	12.1	12.7	12.0

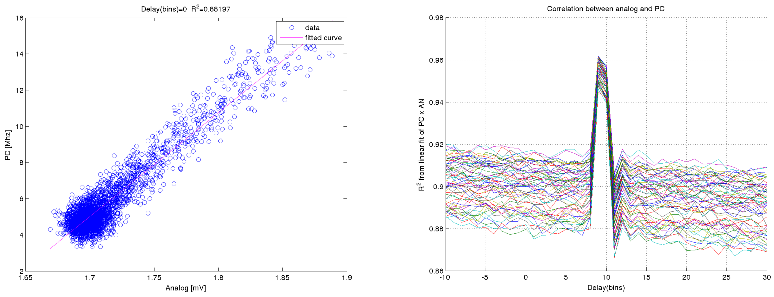

Fig. 1. Sample fitting between the PC and Analog channel in the linear region (left) and lag-correlation as a function of the lag for all profiles in one-hour of measurements (right) are shown.

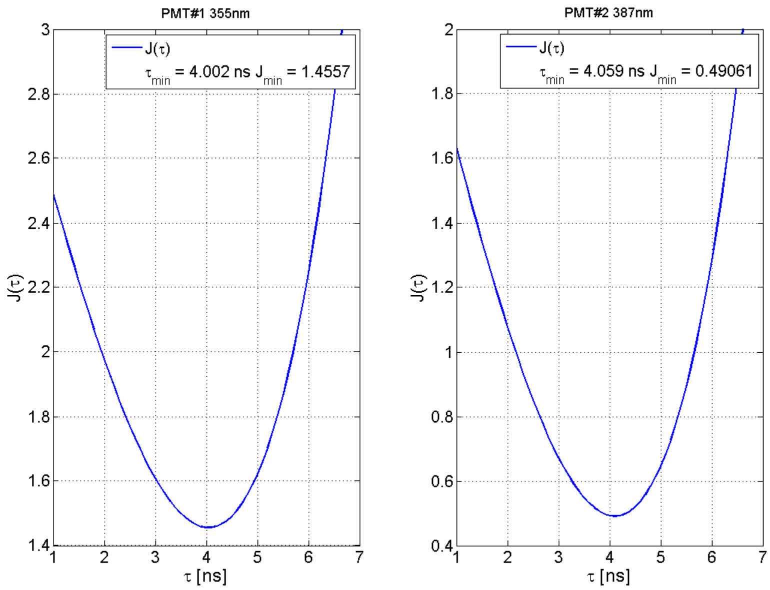

Fig. 2. $J(t,\tau)$ as a function of τ for a sample 1 min profile for the elastic (PMT#1, left) and first Raman (PMT#2, right) channels. The point of minimum was found by fitting a parabola and the values of τ_{min} and $J(t,\tau_{\text{min}})$ are indicated.

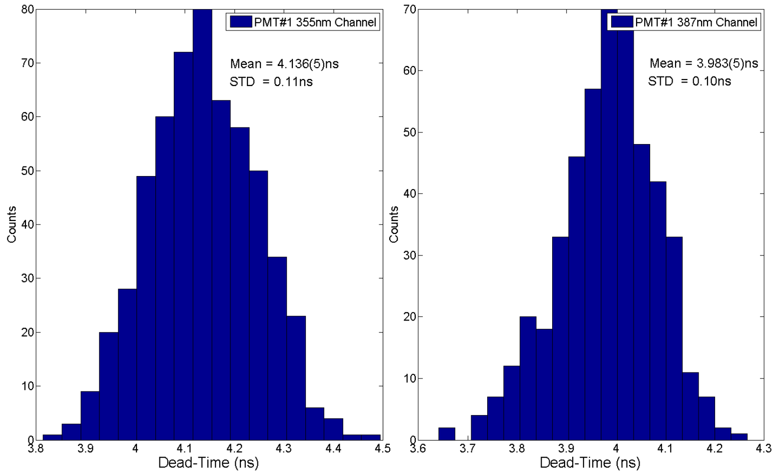

Fig. 3. Histograms of the dead times for the elastic (PMT#1, left) and first Raman (PMT#2, right) channels calculated as shown in Fig. 2 for 580 independent 1 min profiles are shown. The average and standard deviation are indicated.

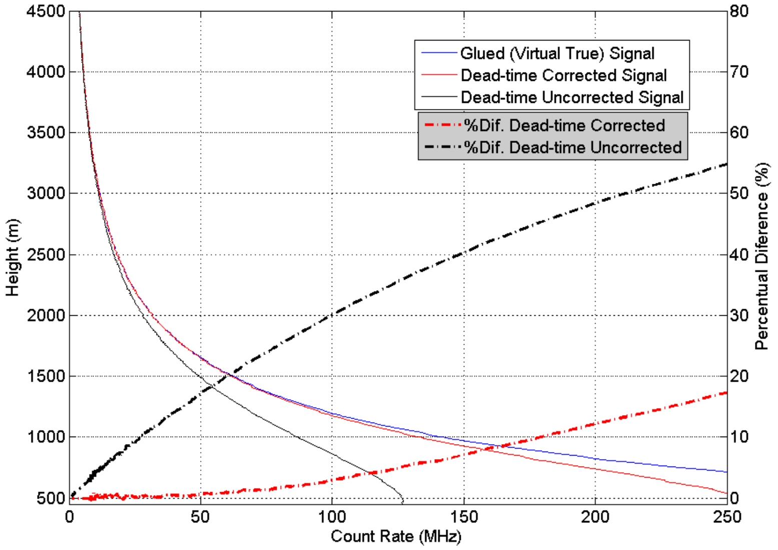

Fig. 4. Corrected (thin red) and uncorrected (thin black) count rates (MHz) from a sample 20 min profile from the elastic channel are shown. The difference (%) between these and the true count rate (glued, thin blue) is given by the red and black dot-dashed lines respectively.

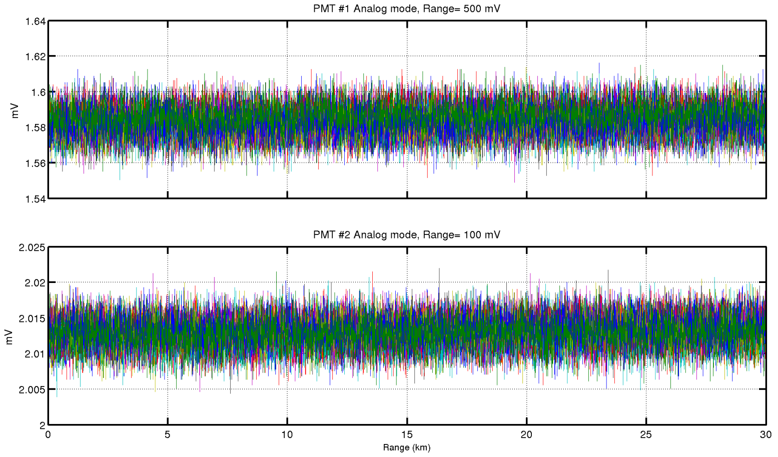

Fig. 5. Analog readings from the two PMT’s during a black-telescope test are shown for 23 profiles of 10 s each.

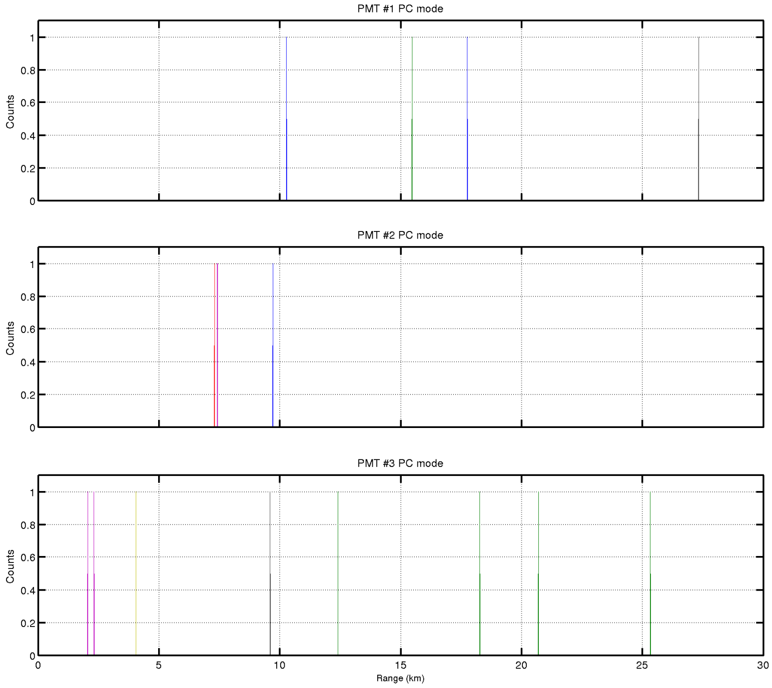

Fig. 6. Photon count readings from the three PMT's during a black-telescope test are shown for 23 profiles of 10 s each.

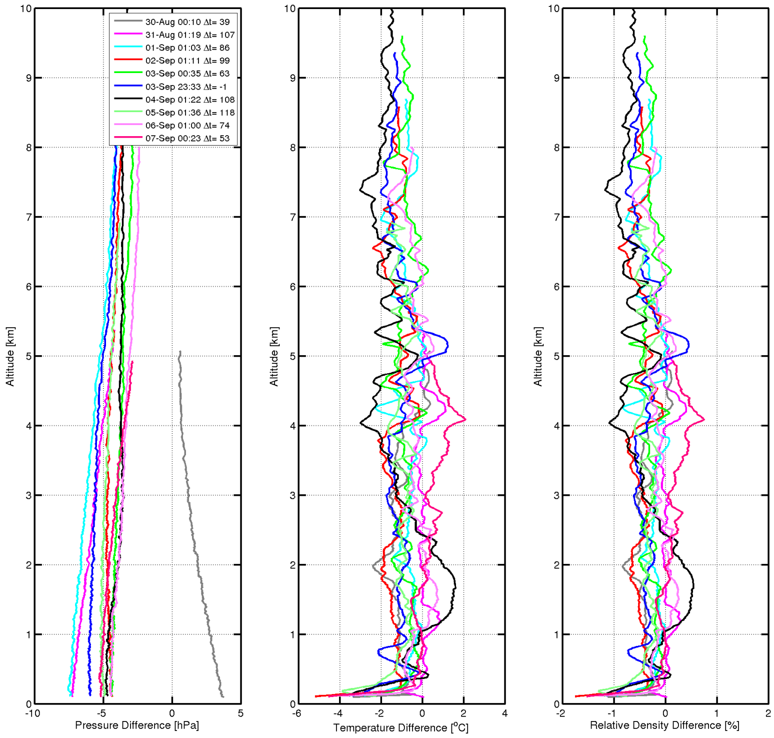

Fig. 7. Absolute pressure (hPa, left), absolute temperature (˚C, center) and relative density (%, right) differences between the Embrapa's and operational's radiosondes are shown. Dates in the legend correspond to the launching time at the Lidar site.

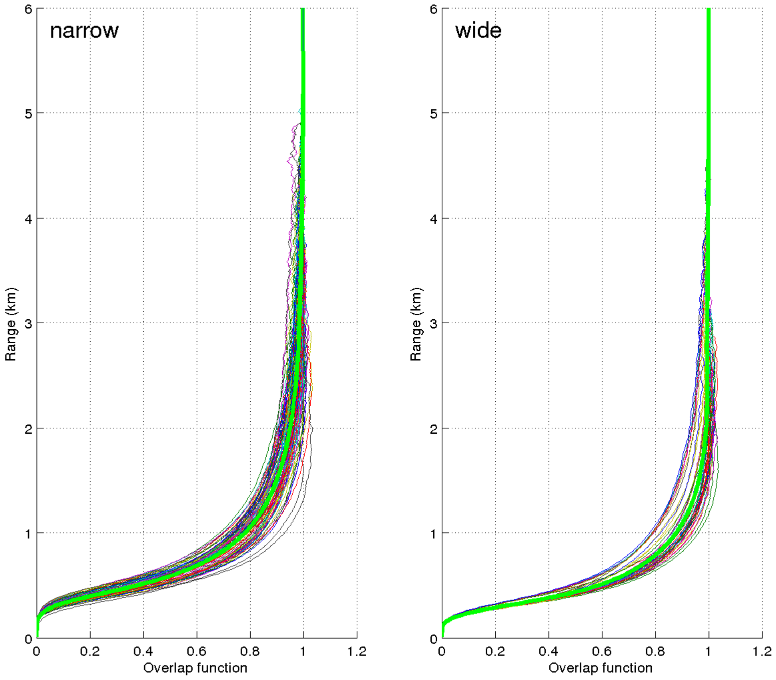

Fig. 8. Overlap function from 45 (90) cloud and fog free nighttime one-hour periods selected after (before) the change in the field stop of the telescope in 1 August 2012.

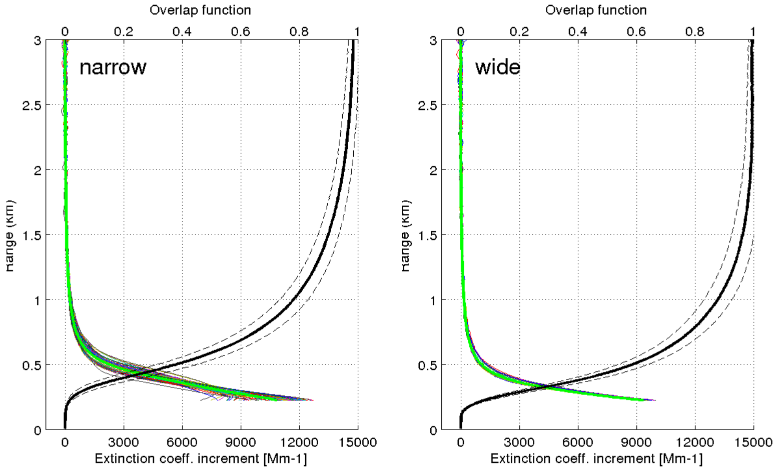

Fig. 9. Black lines indicate the median overlap function and the 95 % confidence level from 45 (90) cloud and fog free nighttime one-hour periods selected after (before) the change in the field stop of the telescope. The colored lines are the contributions to the extinction coefficient, as computed from Eq. (12), and the thick green line is their average.

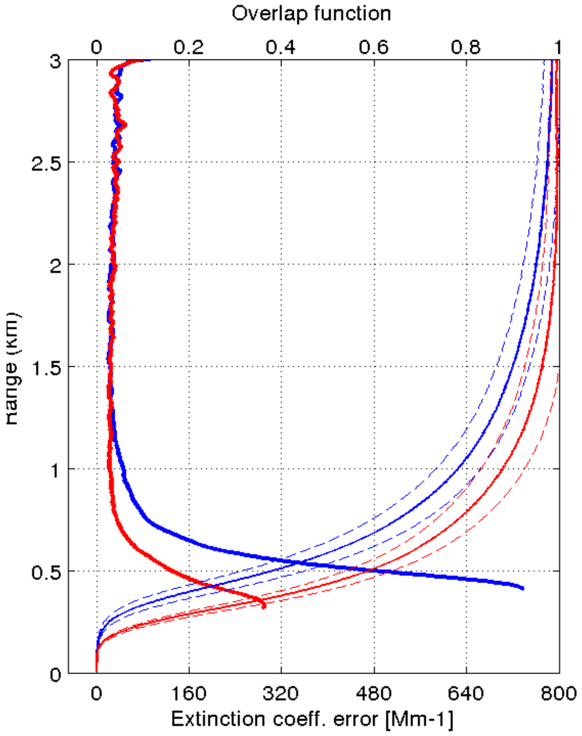

Fig. 10. Estimation of the error in the extinction coefficient from the uncertainty in the overlap function are shown in thick lines. For reference, the overlap functions are shown using thin lines. Red (blue) colors are used for the period after (before) the field stop change.

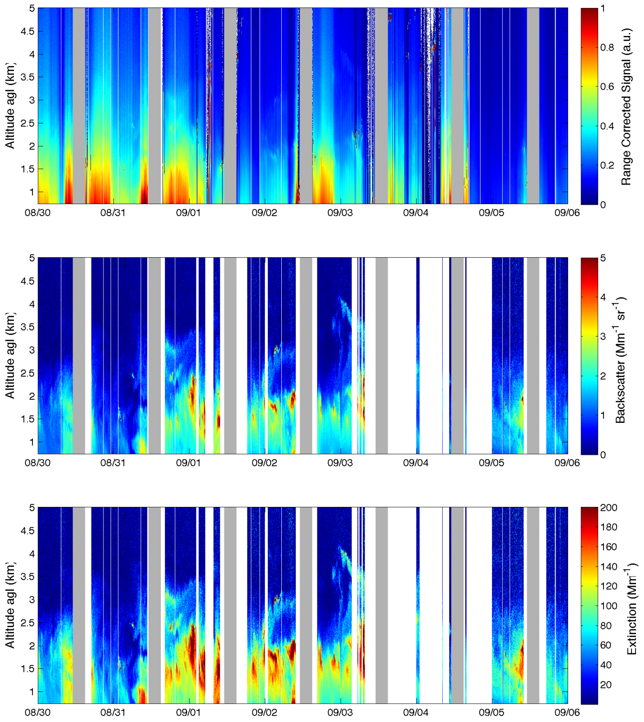

Fig. 11. Range and background corrected signal (top, a.u.), aerosol backscatter (middle, $\mathrm{Mm}^{-1}\,\mathrm{sr}^{-1}$) and extinction (bottom, Mm^{-1}) coefficients obtained from the elastic channels are shown below 5 km from 30 August to 6 September 2011. Inversion assumed a lidar ratio of $55\,\mathrm{sr}^{-1}$. Gray and white regions correspond to local solar noon and clouds respectively.

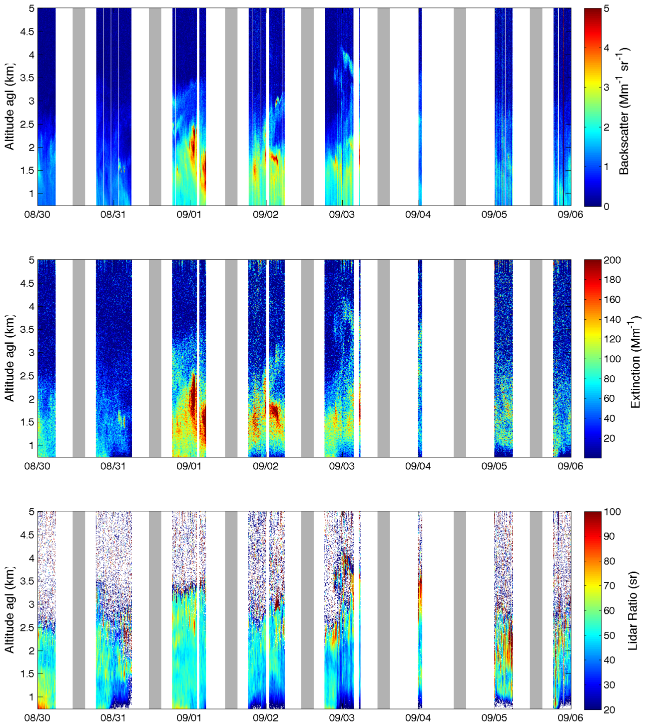

Fig. 12. Aerosol backscatter (top, Mm^{-1} sr^{-1}), extinction (center, Mm^{-1}) and lidar ratio (bottom, sr) obtained from a raman inversion are shown below 5 km from 30 August to 6 September 2011. Gray and white regions correspond to local solar noon and clouds respectively.

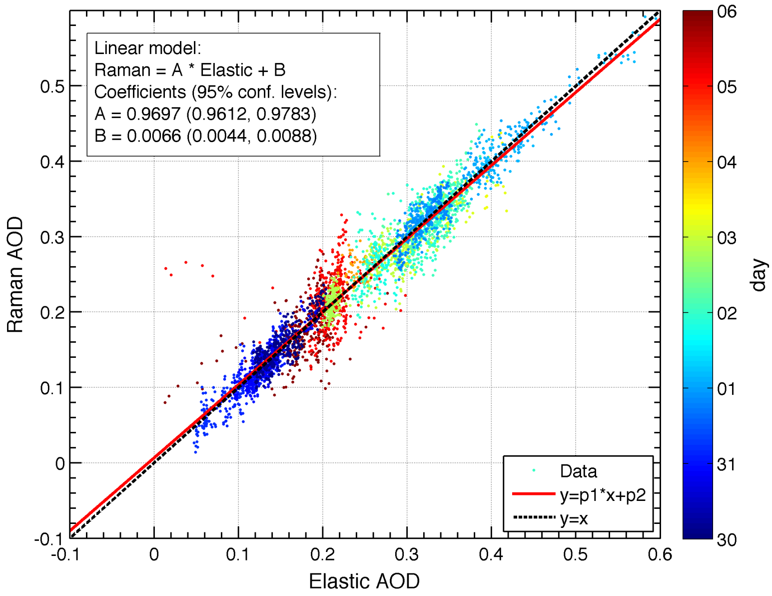

Fig. 13. Aerosol optical depth at 355 nm obtained from the Raman inversion is shown as a function of the optical depth from the Elastic inversion for 4435 nighttime cloud-free 1 min profiles between 30 August and 6 September 2011. Colors indicate day of month. The two lines are the linear regression (continous red) and the reference $y = x$ (dashed).

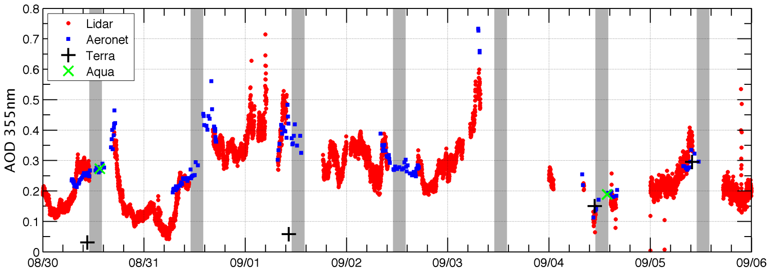

Fig. 14. The time series of aerosol optical depth at 355 nm obtained from the Elastic inversion (red), AERONET (blue), MODIS-Terra (black) and MODIS-Aqua (green) are shown between 30 August and 6 September 2011. Gray regions correspond to local solar noon.

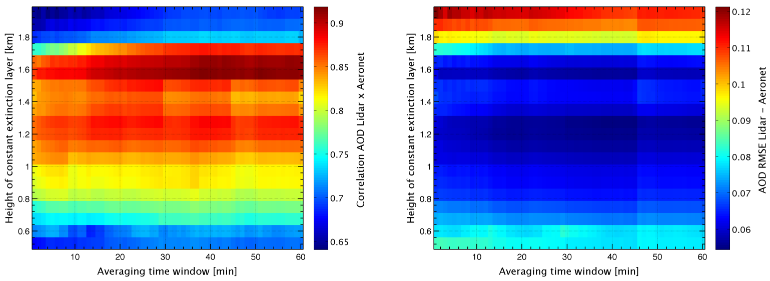

Fig. 15. Time correlation (left) and root mean square error (RMSE, right) between AERONET AOD and elastic Lidar AOD time series are shown as a function of the averaging time window and the height of the constant extinction layer.

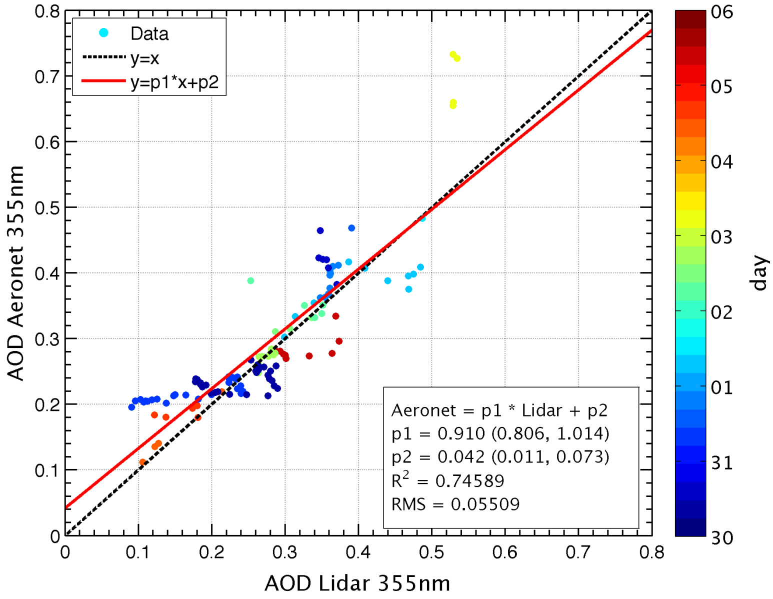

Fig. 16. Aerosol optical depth at 355 nm from AERONET as a function of that obtained from the Elastic inversion is shown for the coincident measurements between 30 and 6 September 2011. Lidar extinction profiles were averaged in a 30 min window and integrated from the reference altitude down to the ground, assuming a constant extinction below 1.3 km.

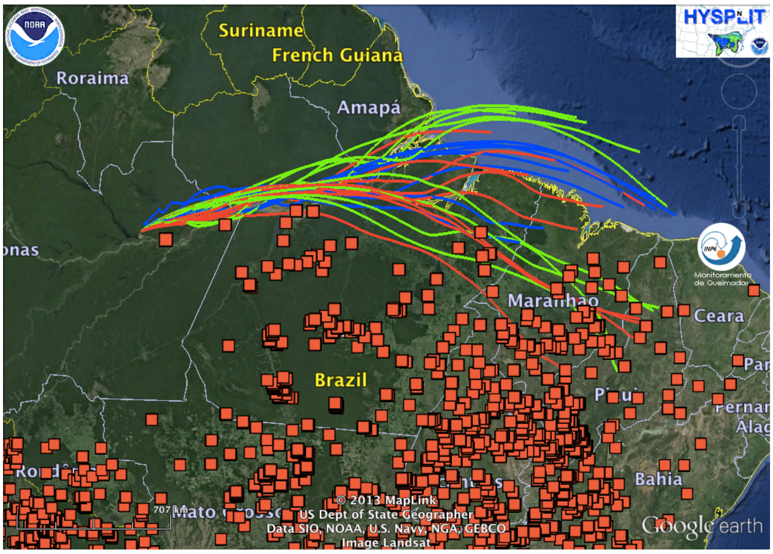

Fig. 17. Back trajectories from the Hysplit model from NOAA and fire spots from Instituto Nacional de Pesquisa Espaciais (INPE)'s fire detection algorithm are shown over a Landsat image of the region obtained with Google Earth. Hysplit was run in ensemble mode, with trajectories starting from 1.5 km on 12:00 UTC 3 September. All fire spots from 30 August to 1 September are shown.

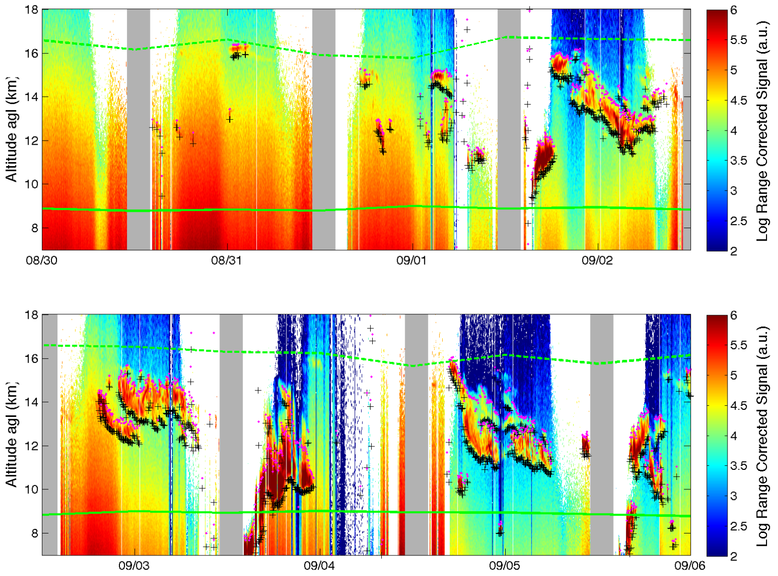

Fig. 18. Logarithm of range corrected signal above 7 km is shown from 30 August to 6 September 2011 divided into two panels for depicting the high clouds. Cloud base (+, black) and top (o, magenta) detected by our algorithm are indicated with markers. Full and dasheed green lines indicate the −25 °C and trotopause heigths calculated from the radiosondes. Gray regions correspond to local solar.